Numerical discreteness and dephasing in high-harmonic calculations in solids

M. Kolesik and J. V. Moloney

Phys. Rev. B **108**, 115433 — Published 27 September 2023

DOI: 10.1103/PhysRevB.108.115433

Numerical discreteness and dephasing in high-harmonic calculations in solids

M. Kolesik and J. V. Moloney
James Wyant College of Optical Sciences, The University of Arizona, Tucson, AZ 85721, U.S.A.

The issue of quantum dephasing in solids subjected to strong, off-resonant excitation continues to challenge our current understanding of nonperturbative extreme nonlinear processes, such as high-order harmonic generation (HHG) and supercontinuum (SC) generation. It has been noted in a number of HHG simulations that realistic-looking spectra, with peak-to-valley contrasts that agree with experimental observations, are only obtained for very short dephasing times. In contrast, simulated spectra attain the character of a structured supercontinuum for longer dephasing times. Using realistic simulations, we establish that this behavior is a manifestation of the necessarily discrete numerical description applied to the continuum of 3D Bloch states. We observe that even when a low-resolution HHG-simulation fails to produce clearly separated harmonic peaks, a properly converged, clearly-defined HHG spectrum can be obtained provided the entirety of the Brillouin zone is sampled with sufficient density. We propose a solution that accelerates the convergence toward the realistic HHG spectra.

I. INTRODUCTION

Solid-state media, from semiconductors to wide-gap laser materials, driven by strong optical fields exhibit pronounced nonperturbative behaviors, as evidenced by highly efficient frequency conversion, supercontinuum generation and higher-order harmonic generation (HHG) [1–4]. Much lower pulse energy relative to HHG in gases enables the efficient generation of attosecond pulses and further extends applications to lightwave driven electronics [5], the optical measurement of band-structure [6–8] and related quantities like Berry curvatures [2, 4] or topological effects [9]. From a physics perspective, a quantitative understanding of the nonlinear interactions in semiconductors has so far been elusive due to two problems: (1) the so-called gauge problem and (2) the dephasing-time problem.

The gauge problem arose in the microscopic modeling from the need to enforce differentiability of complex dipole phases [4, 10]. The practical challenge of implementing this smooth gauge [11] in 3D had proved intractable until recently, and most approaches were limited to modeling HHG along selected 1D high symmetry lines across the Brillouin zone (e.g. [12]). A recent work by Gu et al. [13] showed that by working in the velocity gauge and implementing a full-zone, local unitary transformation algorithm, explicit consideration of dipoles and hence the gauge issue can be avoided and simulations including contributions from the 3D Brillouin zone became tractable. The resolution of the gauge problem made it possible to renew the attack on the second open issue.

The dephasing-time problem [14, 15] shows up in the microscopic Semiconductor Bloch Equations (SBE) [16, 17] when one needs to assume artificially short polarization dephasing times (see e.g. 1.1fs in [12, 18], 2.7fs in [19, 20], 1fs in [21–23], 2.8fs in [24], 4fs in [25], 1.2 fs in [26], ∼1.5 fs in [27], 1/4 of the fundamental cycle in [7]) in order to get agreement with experimental HHG spectra. In simulations with realistic dephasing times, i.e. tens to hundreds fs [28], the simulated spectra look like structured supercontinuua. In contrast, experiments always measure spectra with well-defined harmonic peaks and deep "valleys" in between [1, 12, 29, 30].

As pointed out in several contexts, short dephasing times utilized in the SBE-based simulation may actually be justified [18, 19, 31], especially in systems where correlation effects are important. It is also known that the effective dephasing times may be different between different Bloch states [31, 32]. Thus, given that especially the most frequently used single-time dephasing is merely an approximation which attempts to account for the finite lifetime of electronic states and their coherencies, the fact that a whole range of dephasing times have been used in simulations should not be surprising. However, the number of works that addressed the issue is a witness to the fact that the community has yet to understand what are the reasonable dephasing-time values in cases when the phenomenological dephasing approximation can be reasonably applied in the context of SBE.

Several mechanisms were proposed recently to explain why numerical simulations needed to employ such short dephasing times. For the transmission-geometry experiments, the propagation effects [14] were shown to contribute additional dephasing [33]. Arguing that propagation alone can't be a full solution to the problem because clean HHG spectra can be observed also in the reflection geometry [29], Brown et al. [15] advocate for a real-space perspective on dephasing. Somewhat similar is the approach proposed in Ref. [34], while a very different angle was adopted in [35] where temperature-induced disorder requires averaging. Averaging was also employed in single-cell TDDFT simulations [36]. Important for the experiment-simulation comparisons is the spatio-temporal filtering [37] which greatly reduces the structured-supercontinuum features in the HHG spectra.

The fact that rather different approaches are being explored indicates the importance of the dephasing-time question. Its resolution will enable modeling with realistic parameters, and thus impact a range of applications, such as band structure characterization [6–8], topology-mapping [9], measurements of light-matter couplings [27]

and higher-order nonlinearities [38], extreme solid-state NLO [39], and realistic description of laser materials [40] to name a few.

It is the main goal of this work to demonstrate that realistic HHG spectra can be obtained with short as well as with long dephasing times provided a simulation can account for the HHG contributions from the whole Brillouin zone, and when proper convergence in terms of the zone-sampling is achieved. In other words, an SBE-based HHG simulation which fails to produce clearly defined harmonic peaks at low resolution can eventually converge to a spectrum with sharply separated harmonics even without phenomenological dephasing. The reason that this was not realized earlier, beyond the fact that not many full-zone simulations are being done so far, is that the convergence is slow and requires rather long calculations. We emphasize that this result doesn't contradict any of the previous proposals concerning the dephasing-time issue. What we reveal in this work is not a physical effect but an "additional effective" dephasing mechanism which is intimately connected with the discreteness of the simulation and which coexists with other dephasing channels.

As our secondary but practically important result, we sketch a general approach to deal with the necessity of having sufficiently dense Brillouin-zone sampling. We put forward what we consider to be a first step in designing convergence acceleration for full-zone SBE simulations. Our convergence-acceleration scheme helps to overcome the unavoidable discreteness of the numerical model, and gives rise to a continuum of *effective dephasing times*. In this sense, our insights provide some justification for using artificially short dephasing times in previous SBE-based simulations. However, the "strength" of the grid-induced dephasing varies across the Brillouin zone.

Last but not least, our results shed light onto interference effects responsible for the clean spectra with well-separated harmonic peaks. While the role of destructive interference effects in how HHG-spectra are formed has been recognized (see e.g.[13, 41]), here we show that also the numerical issues connected with the convergence can closely reflect physical properties of the underlying Bloch states as discussed in our Conclusion.

II. SIMULATION-EXPERIMENT COMPARISON

Central to this work is the demonstration that, without any parameter tuning, our simulations produce HHG-spectra which compare well with measurements while utilizing reasonable dephasing times.

We use a structure-gauge-independent SBE solver (sgiSBEs) [13] (see Appendix A for a brief summary) which integrates contributions from the entire Brillouin zone using the time-dependent basis in which every k-vector evolves with the vector potential of the driving pulse, $\vec{k}_t = \vec{k} + \vec{A}(t)$. With $\vec{k}$ sampling the Brillouin zone, the time-dependent density matrix $\rho(\vec{k}|t)$ is obtained for each initial Bloch-state given by $\vec{k}$, and all these contributions are added up in calculating the total induced current density (see Appendix B for details). It has been recognized that accurate integration over the entire zone is necessary for the convergence and preservation of the system's symmetry. However, most of the works which include the full zone are based on time-domain density-functional theory (TDDFT). In the meantime, full-zone SBE-based simulations specifically in three-dimensional materials are still rare (see Ref.[14] for a notable exception). Moreover, little attention was paid to convergence which to the best of our knowledge was not studied in detail.

There are a couple of advantages of the sgiSBEs method important for the current purpose. The first is that neither dipole moments nor Berry connections appear in the algorithm. Moreover, in line with the postulates of quantum theory, the Bloch-state phases are irrelevant for any observable, and our algorithm is designed to be agnostic in this sense — it works with arbitrary Bloch-state phases and no smooth structure-gauge preparation is needed.

Thanks to absence of pre-calculated data for dipoles and/or Berry connections, the simulations require no interpolation and there are no finite-difference approximation used. The absence of interpolation and finite-difference approximations helps to keep the noise-floor of the whole calculation very low (see simulated spectra in Ref.[13]), which is important when one studies the convergence w.r.t. the sampling of the Brillouin zone.

To show that our simulation can produce results in good agreement with experiments, we model some of the measurements reported in [29]. It is important to note that once we fix the driving-pulse properties and the sample orientation as in the experiment, the sole parameter in the whole simulation which can be adjusted is the dephasing time T_2. Apart from a few comparative simulation runs, we employ T_2 longer than the duration of the excitation pulse, and in such a regime the impact of the dephasing time does not depend on its precise value.

Mimicking the setup from Ref. [29], we assume a GaAs sample irradiated by a 3.5μm wavelength, 60 fs duration, pulsed Gaussian beam giving rise to a in-material peak amplitude of $E_0 = 10$ MV/cm. Two experiment geometries are examined in what follows. Simulation A represents a GaAs sample with facet orientation 100 and the field polarization along 110. Simulation B is for a sample with orientation 011 and the field oscillating at 45 deg with respect to crystal axis 100. To exclude propagation effects, we calculate the Reflection-geometry High-Harmonic Spectra (RHHG).

It is important to include spatial filtering [37] before a comparison with measured data can be made. Here, "spatial" refers to the (Gaussian) distribution of peak intensities driving the material at different locations across the focal spot. The "filtering" refers to the fact that in

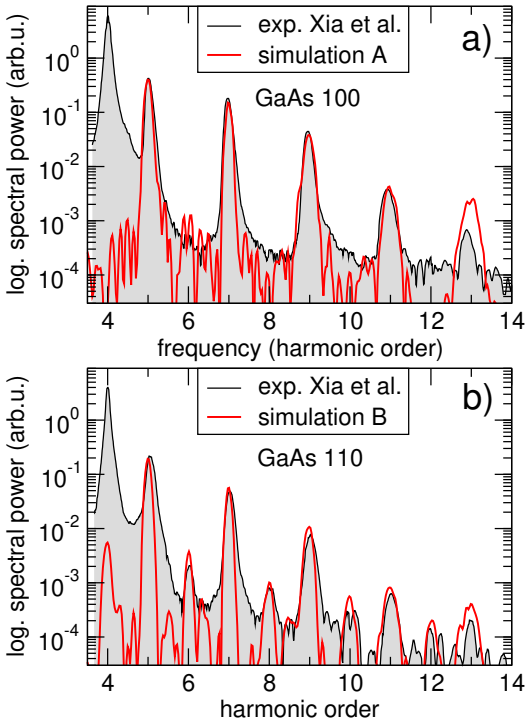

FIG. 1. Comparison of simulated spectra (thick red line) to measurements by Xia et al. (gray-shaded area). Sets representing experiments were obtained by digitizing reflection HHG spectra from figures 2 and 6 in Ref. [29]. Note that the experimental peak at order four is fluorescence, not HHG.

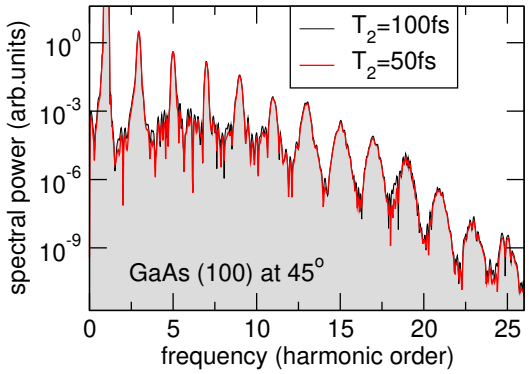

FIG. 2. HHG spectra, simulated in the reflection geometry, with different dephasing times; Result for $T_2 = 100$fs is shown as a gray-shaded area, and thin red line represents $T_2 = 50$fs.

experiments the spectra are observed in the far field, so it is what we need to calculate. We therefore sample the Gaussian beam profile with 15 (30 to confirm convergence) points and evaluate the induced current response at each. The resulting far-field is obtained from the discrete Hankel transform [42] as a coherent weighted sum of results gotten for the spatial-grid points (note that this is a standard procedure in pulse-propagation simulation [43]). Finally, we evaluate the RHHG spectrum from the current response in the far field.

In this work, the material model used by our simulator is the tight-binding Hamiltonian for GaAs using ten spin-degenerate bands in the sp^3s^* approximation, with the k-dependent Hamiltonian and the tight-binding parameters taken from [44]. We have previously shown [45] that the tight-binding models of GaAs and ZnSe which account for the spin-orbit coupling are capable of reproducing the high-harmonic experiments of Ref. [29], and they also exhibit second-order nonlinear coefficients that compare well with measurements. This gives us confidence that the tight-binding models capture the essential physics needed for the present study. However, here we use the spin-degenerate version of the GaAs material model, which only requires half as many bands, namely ten. This model is chosen for its computational efficiency as this work required a large number of simulations for parameter scans (e.g field amplitude, polarization) and extensive convergence studies including very dense sampling of the Brillouin zone. Despite the relative simplicity of the material model, say compared to DFT-based descriptions, we are able to demonstrate that the RHHG measurements reported in [29] can be closely reproduced.

Figure 1 compares the experimental RHHG from Ref. [29] to our simulations. The results agree nicely with the experiment in terms of the relative strength of the harmonic peaks. Our simulation also correctly reflects the crystal symmetry as even harmonics appear weaker and only for the 011 sample-orientation.

Data shown in Fig. 1 were obtained for a dephasing time $T_2 = 100$fs. Figure 2 demonstrates that as long as T_2 is comparable to or longer than the pulse duration, the simulated RHHG spectrum changes very little with T_2. We thus come to a conclusion that our HHG simulation does not suffer from the infamous dephasing-time problem; spectra simulated with physically reasonable T_2 values exhibit well-formed harmonic peaks separated by deep valleys, and they compare will with experiments.

III. BRILLOUIN-ZONE SAMPLING AND CONVERGENCE

The fact that a number of published simulations used very short T_2 in order to produce reasonably looking spectra begs the question about what is different in this case, and the answer has two parts. First, the integration of the radiation produced over the entire Brillouin zone is necessary to obtain HHG comparable to experiments. Second, the Brillouin-zone sampling must be sufficiently dense to ensure numerical convergence, and this becomes more challenging for longer dephasing times. While the issue of convergence may seem merely technical, there is physics behind it. Unlike in HHG in gases where the initial and final electronic states are discrete, in the solid state we deal with continuum-to-continuum processes which are more challenging to model.

Figure 3 illustrates the convergence of the RHHG spec-

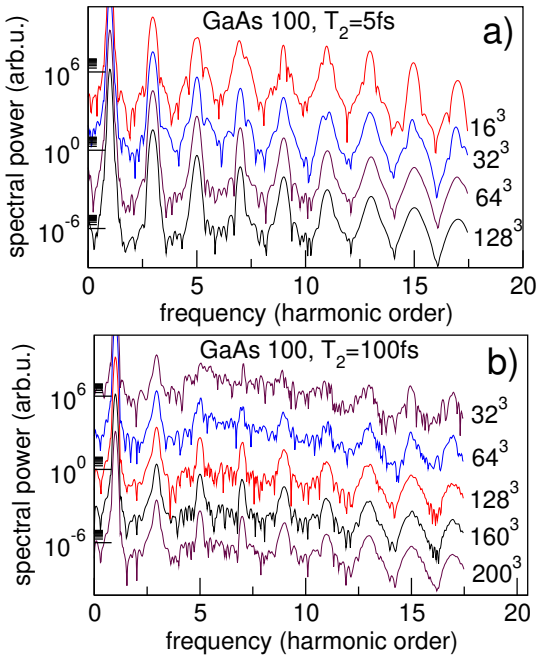

FIG. 3. Simulated RHHG spectra for increasing density of the sampling in the reciprocal space. Labels to the right of each curve represent the number of sampling points distributed over an equidistant grid aligned with the reciprocal basis vectors. A) The convergence is faster for a short $T_2 = 5$fs than B) for a longer $T_2 = 100$fs.

trum while the number of sampling points in the Brillouin zone increases. To demonstrate that reaching the convergence is easier for a very short dephasing time, panel a) reports the results for $T_2 = 5$fs. In this case, the peak-to-valley contrast is strong already for a coarse sampling, and a converged spectrum is obtained at 64^3 points.

The top curve in Fig. 3b shows that for a more realistic dephasing time of $T_2 = 100$fs, and even with the spatial filtering (far-field calculation), a coarsely sampled Brillouin zone results in a spectrum that lacks well-defined harmonic peaks, especially for frequencies above order five. As the number of sampling points increases (top to bottom), the harmonic peaks stabilize first, while it takes a denser discretization to achieve suppression of the spectral power between the harmonic peaks. This behavior suggests that the spectral minima form by superposition of contributions with "random" phases which require a large number of samples so that they can eventually average out. For the harmonic peaks, the mechanism is different in that the contributions to a given peak which originate from different parts of the Brillouin zone tend to be in-phase.

To appreciate how the spread of complex phases gives rise to spectral minima, a numerical experiment is illustrated in Fig. 4. We generated one thousand k-vectors scattered randomly over the Brillouin zone, and evaluated the current-density for the corresponding initial Bloch states. From each individual response we filtered

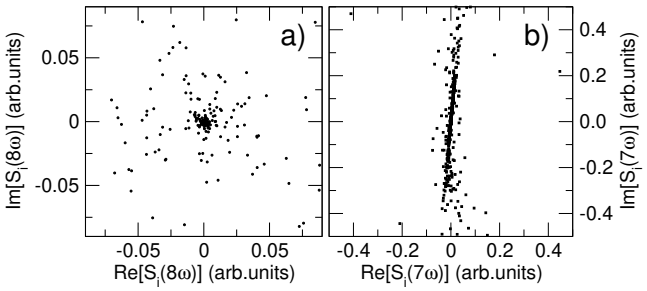

FIG. 4. Complex spectral amplitudes of the current density for a random set of k-vectors representing the initial Bloch states. Frequency band around the 8th harmonic of the fundamental frequency is shown in a), and b) shows the corresponding amplitudes for the 7th harmonic.

out narrow bands around the 7th harmonic and the spectral minimum between this and the 9th harmonics, corresponding to a peak and a spectral minimum, respectively. Then we compared the individual spectral amplitudes shown in the scatter plots of Fig. 4. While in both bands the spread of the contributions is significant, there is a clear difference. The complex phases appear random around a minimum of HHG as illustrated in panel a). In contrast, the phases are much more similar for the HHG-peak (b). In other words, a HHG minimum occurs not because the material does not respond at that frequency, but because there is a continuum of responses that lack coherence.

The slow convergence of the simulated HHG spectrum with the increasing number of points sampling the Brillouin zone means heavy computational cost, which may hit especially hard the SBE-based approaches that rely on first principles for their material models. It is also unfortunate that most of the numerical effort goes to getting right the least interesting part(s) of the spectrum, i.e. the minima between harmonic peaks.

IV. CONVERGENCE ACCELERATION

Armed with this understanding, and having seen that simulations (both here and previously published) with artificially fast dephasing tend to obtain reasonable harmonic peaks, we can ask if such simulations do "something right." The asnwer might be affirmative in the sense that artificial dephasing times in fact mimick an accelerated convergence w.r.t. the sampling of the Brillouin zone. As a first step in exploring this idea, we propose here what could be characterized as convergence-acceleration via artificial dephasing. Instead of the traditional dephasing step

$$\rho_{ab}(\mathbf{k}, t) \leftarrow \rho_{ab}(\mathbf{k}, t) \exp[-\Delta t/T_2] \qquad (1)$$

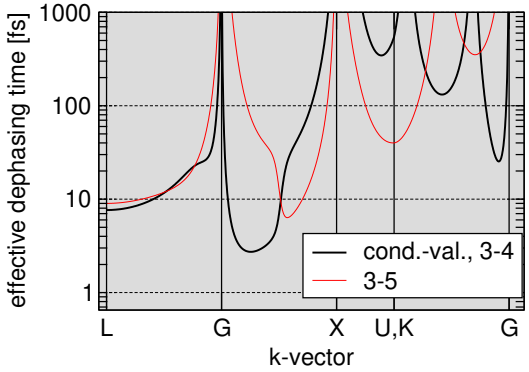

FIG. 5. Effective dephasing time between the valence band (label 3) and the first (4) and second (5) conduction bands calculated for a Brillouin zone sampled with 32^3 grid-points. Regions with long dephasing times correspond to where the relative group velocities between the bands vanish or are small.

with the same dephasing time T_2 for all bands, one can derive a still crude but better approximation as

$$\rho_{ab}(\mathbf{k},t) \leftarrow \rho_{ab}(\mathbf{k},t)\prod_{d=1}^{3}\mathrm{sinc}\left[\Delta t/\tau_{ab}^{(d)}\right] \qquad (2)$$

where the effective band- and grid-spacing-dependent dephasing time is

$$\left(\tau_{ab}^{(d)}\right)^{-1} = \frac{1}{2N}\mathbf{b}_d\cdot\left|\frac{\partial\epsilon_b(\mathbf{k})}{\partial\mathbf{k}} - \frac{\partial\epsilon_a(\mathbf{k})}{\partial\mathbf{k}}\right| \qquad (3)$$

with $\mathbf{b}_d$ standing for the reciprocal lattice vector and N representing the number of grid points taken equal in each lattice-vector direction. This formula suggests that this artificial dephasing is faster between bands with different group velocities, but should affect nested bands much less. While this effect is born out of the discreteness of the Brillouin-zone grid, its momentum-dependence together with a broad range of dephasing times are akin to those calculated from first principles [32].

To illustrate the broad value-range of $\tau_{ab}^{(d)}$ together with their band-dependence, Fig. 5 shows a couple of them calculated for a modestly sampled Brillouin zone with thirty two points in each direction. It is evident that the dephasing times can be drastically different between different pairs of bands. Perhaps more importantly, the figure shows that those states where the relative group velocities vanish are least affected by this convergence-acceleration scheme. The Γ point is an example of such a high-symmetry point; the states from its close vicinity "will be left alone" because of their long τ, while states further away will be preferentially damped on smaller grids. As a result, the scheme, when applied on a smaller grid, emphasizes the states with spectral contributions that are destined to survive in the converged result obtained from a densely sample zone.

The derivation of what can be termed discreteness- or grid-induced effective dephasing is shown in Appendix C. It is based on the intuitive assumption that the fastest complex-phase variations of the density matrix are caused by the k-dependent band energies. The grid-induced dephasing is a result of the integration over a small volume around a sampling point in the Brillouin zone, and doing this with these phase variations included. Here we would like to demonstrate that the grid-induced dephasing indeed accelerates the convergence of the simulated spectrum.

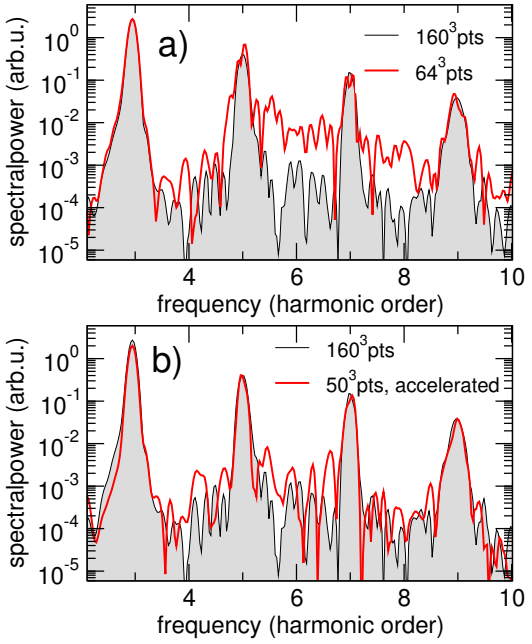

FIG. 6. Convergence acceleration via discreteness-induced effective dephasing. Reference panel a) shows the same data as in Fig. 3b, zooming in on a detail illustrating the slow convergence with the increasing number of sampling points. Panel b) compares the same fine-grid result (gray-shaded area) with the spectrum obtained with the inclusion of the grid-induced dephasing.

Figure 6 shows the effect of the accelerated convergence for a section of the spectrum in Fig. 3b. The top panel is for a reference and shows the difference between the spectra simulated with $N = 160$ and $N = 64$ grid points along each reciprocal lattice direction. The relevant feature here is the elevated spectrum "floor" between the harmonic peaks for the coarser grid. The bottom panel compares the same fine-grid results with a simulation on a much coarser grid ($N = 50$, 33× less effort) but employing the grid-induced dephasing term (3),(2). It is evident that the two spectra are much closer, with improvement especially evident for spectral minima. This is an encouraging observation, because it demonstrates that the brute-force Brillouin-zone sampling may not be the only way to a converged result.

V. CONCLUSION

In a stark contrast to a number of previous works, we have demonstrated that an SBE-based simulation of HHG from a solid-state medium does not need to rely on unrealistic, short dephasing times in order to produce spectra comparable with experiments. However, it is necessary to integrate contributions from the entire Brillouin zone and ensure that the sampling of the reciprocal space is fine enough to achieve the sharp peak-valley contrast consistent with experimental observations. The physical reason for the convergence being rather slow is that contributions to HHG originate from continuum-to-continuum transitions and they vary rapidly with the location inside the Brillouin zone.

The computational cost of achieving converged simulated spectra can be significant, and especially challenging for SBE-based simulations utilizing first-principle material models. We propose that a more accurate sampling, accelerated convergence, and thus substantially lower costs can be achieved by a more accurate treatment of the Brillouin-zone discretization. As a first step in this direction we put forward the idea of grid-induced effective dephasing. While only a first, crude approximation, it shows significantly accelerated convergence, and we trust this approach can be further improved.

The grid-induced dephasing mechanism is a purely numerical construct, which does not add to or modify the physics of the system in any way. It only speeds-up the approach to the converged HHG spectrum, and thus helps to reduce the required numerical effort. Nevertheless, the scheme does reflect certain physical properties of the simulated material; The way the effective dephasing times depend on the band-energies identifies those Bloch states that are most susceptible to the convergence slow-down. For example, the grid-induced dephasing is weak between nested bands where the excitation's group-velocities are similar. In contrast, bands with very different group velocities carry wavepackets that collide at higher relative velocities which is reflected in the shorter dephasing time for the given pair of bands. This kind of "selective damping" is in line with the role of spectral singularities [46] when regions with zero relative group velocities end up more pronounced (in our case less damped) in the spectrum.

Another analogy can be identified with the finite-size effects. As the simulation gets better and better resolved in terms of the number of grid points populating the Brillouin zone, whether with or without acceleration, it represents bigger and bigger sample of the material with more and more atoms. In the process, the simulated density of Bloch states increases and there are more contributions to each "valley" of a HHG spectrum giving rise to a more complete destructive interference. The result is a "cleaner" HHG spectrum. Very much analogous behaviors were identified in correlated systems (e.g. [47]), where electron-electron correlations coupled with finite-size effects can transform a supercontinum-like spectrum of a small system to a HHG spectrum with sharply defined peaks for bulk.

The issues discussed in this work are rooted in the the necessarily discrete numerical representation of what is a continuum of states needed to describe the dynamics in a solid-state medium. This is why our insights should be useful in a number of situations involving off-resonantly driven solids where integrals over the Brillouin zone represent observable quantities. An improvement beyond the current grid-induced dephasing scheme will therefore be important for applications across the solid-state optical physics.

ACKNOWLEDGMENTS

Authors acknowledge the support from the Air Force Office for Scientific Research under grants no. FA9550-22-1-0182 and FA9550-21-1-0463.

APPENDIX A: STRUCTURE-GAUGE INDEPENDENT SBE SOLVER

For the Reader's convenience, this Appendix gives a brief overview of the numerical approach put forward in Ref.[13]. The algorithm underlying the structure-gauge independent SBE solver (sgiSBEs) derives from the density matrix evolution equation in the co-moving basis. The $\mathbf{k}$-dependent Hamiltonian becomes time-dependent in the velocity gauge, and under the assumption of minimal coupling,

$$H(\mathbf{k}) \to H(\mathbf{k}_t) \quad \text{where} \quad \mathbf{k}_t = \mathbf{k} - \mathbf{A}(t) \ . \tag{4}$$

Let us denote $\{|a\mathbf{k}_t\rangle\}$ the instantaneous basis of this time-dependent Hamiltonian, assuming that it is orthonormal, so we have $\langle a\mathbf{k}_t|b\mathbf{k}_t\rangle = \delta_{ab}$ and therefore also

$$(\partial_t\langle a\mathbf{k}_t|)|b\mathbf{k}_t\rangle + \langle a\mathbf{k}_t|(\partial_t|b\mathbf{k}_t\rangle) = 0 \ . \tag{5}$$

If, for now, we ignore the phenomenological dephasing then the equation of motion for the density matrix reads

$$i\partial_t\rho(\mathbf{k},t) = H(\mathbf{k}_t)\rho(\mathbf{k},t) - \rho(\mathbf{k},t)H(\mathbf{k}_t) \ , \tag{6}$$

which is stated independently of the particular basis used. The elements of the density matrix in the instantaneous eigen-basis are

$$\rho_{ab}(\mathbf{k},t) = \langle a\mathbf{k}_t|\rho(\mathbf{k},t)|b\mathbf{k}_t\rangle \ , \tag{7}$$

and depend on time in two ways; because of the density-matrix evolution *and* due to time-dependence of the basis. The double-dependence on time gives two kinds of terms in

$$\begin{aligned} i\partial_t\rho_{ab}(\mathbf{k},t) = {} & \langle a\mathbf{k}_t|i\partial_t\rho(\mathbf{k},t)|b\mathbf{k}_t\rangle \\ & + i\langle a\mathbf{k}_t|\rho(\mathbf{k},t)(\partial_t|b\mathbf{k}_t\rangle) + i(\partial_t\langle a\mathbf{k}_t|)\rho(\mathbf{k},t)|b\mathbf{k}_t\rangle \ . \end{aligned} \tag{8}$$

This equation leads directly to the SBE in the co-moving basis. Using

$$\partial_t|a\mathbf{k}_t\rangle = \partial_{\mathbf{k}_t}|a\mathbf{k}_t\rangle.\partial_t\mathbf{k}_t = \partial_{\mathbf{k}_t}|a\mathbf{k}_t\rangle.\mathbf{E}(t) \tag{9}$$

one obtains the SBE,

$$\begin{aligned}(i\partial_t - \epsilon_{nm}(\mathbf{k}_t))\rho_{nm}(\mathbf{k};t) = \\ \mathbf{E}(t)\sum_a (\rho_{na}(\mathbf{k};t)\mathbf{d}_{am}(\mathbf{k}_t) - \mathbf{d}_{na}(\mathbf{k}_t)\rho_{am}(\mathbf{k};t))\end{aligned} \tag{10}$$

where the dipole-moment matrix and the band-energy differences are

$$\mathbf{d}_{am}(\mathbf{k}_t) = \langle a\mathbf{k}_t|i\partial_{\mathbf{k}_t}|m\mathbf{k}_t\rangle \ , \epsilon_{nm}(\mathbf{k}_t) = \epsilon_n(\mathbf{k}_t) - \epsilon_m(\mathbf{k}_t) \ . \tag{11}$$

Obviously, a tacit assumption underlying the above evolution description is that $|m\mathbf{k}\rangle$ can be made differentiable w.r.t. $\mathbf{k}$ at least locally.

Once the SBE is solved, for all initial $\mathbf{k}$, the total current density can be calculated as

$$\mathbf{j}(t) = \sum_{mn}\int \frac{d\mathbf{k}}{(2\pi)^3}\langle n\mathbf{k}_t|\partial_{\mathbf{k}_t}h(\mathbf{k}_t)|m\mathbf{k}_t\rangle\rho_{mn}(\mathbf{k};t) \ . \tag{12}$$

This says that the observed induced current is expressed as an integral which requires to calculate $\rho_{mn}(\mathbf{k};t)$ for all initial $\mathbf{k}$ running over the entirety of the Brillouin zone.

The above derivation makes it evident that the "dipole and Berry-connection terms" in SBE originate in the time-dependence of the Hamiltonian eigen-basis.

To solve the evolution in a way that eliminates the need to calculate (and use) the dipole moments and the Berry connections, we go back to the equation (6).

Assuming that $\rho(\mathbf{k};t_i)$ has been calculated for a time t_i, one integration step "evolving" it to the next time t_{i+1} is realized under the assumption that $\Delta = t_{i+1} - t_i$ is small enough so that the Hamiltonian in this interval can be approximated by the constant $H(\mathbf{k}_i)$ (denote $\mathbf{k}_i = \mathbf{k} - \mathbf{A}(t_i)$),

$$\rho(\mathbf{k};t_{i+1}) = e^{-iH(\mathbf{k}_i)\Delta}\rho(\mathbf{k};t_i)e^{+iH(\mathbf{k}_i)\Delta} \ . \tag{13}$$

This is a basis-free expression of one integration step. To write the same in the instantaneous Hamiltonian basis at each time, sandwich the above between the eigenvectors of the Hamiltonian at t_{i+1},

$$\rho_{mn}(\mathbf{k};t_{i+1}) = \langle m\mathbf{k}_{i+1}|\rho(\mathbf{k},t_{i+1})|n\mathbf{k}_{i+1}\rangle = \langle m\mathbf{k}_{i+1}|e^{-iH(\mathbf{k}_i)\Delta}\rho(\mathbf{k};t_i)e^{+iH(\mathbf{k}_i)\Delta}|n\mathbf{k}_{i+1}\rangle \tag{14}$$

and insert resolution of unity twice, using the basis at t_i,

$$\rho_{mn}(\mathbf{k};t_{i+1}) = \sum_{a,b}\langle m\mathbf{k}_{i+1}|e^{-iH(\mathbf{k}_i)\Delta}|a\mathbf{k}_i\rangle\langle a\mathbf{k}_i|\rho(\mathbf{k};t_i)|b\mathbf{k}_i\rangle\langle b\mathbf{k}_i|e^{+iH(\mathbf{k}_i)\Delta}|n\mathbf{k}_{i+1}\rangle \tag{15}$$

to get

$$\rho_{mn}(\mathbf{k};t_{i+1}) = \sum_{a,b}\langle m\mathbf{k}_{i+1}|a\mathbf{k}_i\rangle e^{-i\epsilon_a(\mathbf{k}_i)\Delta}\rho_{ab}(\mathbf{k};t_i)e^{+i\epsilon_b(\mathbf{k}_i)\Delta}\langle b\mathbf{k}_i|n\mathbf{k}_{i+1}\rangle \ . \tag{16}$$

This integration step can be interpreted as an operator splitting scheme:

Step I: One multiplies the density matrix, element-wise,

$$\rho^{(1)}_{ab} = e^{-i\epsilon_a(\mathbf{k}_i)\Delta}\rho_{ab}(\mathbf{k};t_i)e^{+i\epsilon_b(\mathbf{k}_i)\Delta} \ . \tag{17}$$

This step is a solution that includes the diagonal terms in the SBE system (10), and realizes the evolution of the density matrix under the action of the Hamiltonian in its own basis.

Step II: One multiplies with a unitary matrix from the left and its adjoint from the right,

$$\rho_{mn}(\mathbf{k};t_{i+1}) = \sum_{a,b}U^{(i)}_{ma}\rho^{(1)}_{ab}(U^{(i)})^\dagger_{bn} \tag{18}$$

where $U^{(i)}$ transforms from the basis at time t_i to the basis at time t_{i+1}:

$$U^{(i)}_{ma}(\mathbf{k}) = \langle m\mathbf{k}_{i+1}|a\mathbf{k}_i\rangle. \tag{19}$$

This second step achieves in one go what the integration of the dipole terms in the SBE system (10) would do, namely transform the current density matrix into the eigen-basis at time t_{i+1}. Unlike in ODE integration of (10), the unitarity of the transformation is guaranteed here.

The algorithm (16) is independent of the structure gauge, i.e. independent of the assignment of complex phases to Bloch states. The unitary transform (19) between the bases at the different times can be constructed with arbitrary complex phases assigned to the Hamilto-

nian eigenstates, and this is a distinct advantage because we can utilize the eigenstates as delivered by an eigensystem solver and avoid the construction of the smooth (w.r.t. $\mathbf{k}$) phase. Moreover, evaluation of the dipole moments and/or Berry connections is not needed.

Since at the end of each integration step the density matrix is in the eigen-basis for the current time, the dephasing step can be added as in Eqn.(1).

APPENDIX B: BRILLOUIN-ZONE SAMPLING

The important feature of the sgiSBEs method is that for any given initial $\mathbf{k}$, $\rho_{mn}(\mathbf{k}|t_i)$ and its contribution to the observable current are calculated independently. To add-up all contributions to the induced current, one must sample all possible $\mathbf{k}$ on a grid.

To approximate the integral (12) over the Brillouin zone, we sample the reciprocal space on an equidistant grid aligned with the basis vectors of the reciprocal lattice:

$$\mathbf{k}^{(s)} = \frac{s_1}{N}\mathbf{b}_1+\frac{s_2}{N}\mathbf{b}_2+\frac{s_3}{N}\mathbf{b}_3 \ , \ \ s_i = 0,1,2,\ldots,N-1 \quad (20)$$

where the triple index $s \equiv (s_1, s_2, s_3)$ and N represents the number of grid points along each reciprocal lattice direction. The straightforward approximation for the integral (12) with the above grid is

$$\mathbf{j}(t)=\sum_{mns}\frac{V_s}{(2\pi)^3}O_{nm}\left(\mathbf{k}^{(s)}-\mathbf{A}(t)\right)\rho_{mn}(\mathbf{k}^{(s)}|t) \ , \quad (21)$$

where V_s stands for the grid-cell volume centered on point $\mathbf{k}^{(s)}$, and where we introduced a shorthand for the observable operator matrix element,

$$O_{nm}\left(\mathbf{k}-\mathbf{A}(t)\right) = \langle m\mathbf{k}_t|\partial_{\mathbf{k}_t}h(\mathbf{k}_t)|n\mathbf{k}_t\rangle \ . \quad (22)$$

It is important for the numerical accuracy that grid (20) is invariant under the action of the material symmetries. It means that if g is a symmetry element, every $g\mathbf{k}^{(s)}$ also belongs to the same grid or is equivalent to one of the grid points in (20). This property can be proven with the help of the explicit vector representation of the zinc-blende symmetry.

APPENDIX C: CONVERGENCE ACCELERATION

In some instances, the convergence of (21) with $N \to \infty$ is rather slow due to the fact that the complex phases in the integrand vary fast with $\mathbf{k}$. In an attempt to take such phase variations into account, albeit only partially at this time, let us rewrite the observable (12) as

$$\mathbf{j}(t)=\sum_{mns}\frac{V_s}{(2\pi)^3}\int_{V_s}\frac{d\mathbf{k}}{V_s}O_{nm}(\mathbf{k}-\mathbf{A}(t))\rho_{mn}(\mathbf{k}|t) \ , \quad (23)$$

where each of the integrals is over the volume V_s centered at $\mathbf{k}^{(s)}$. Assuming that in terms of the phase variation upon deviation from $\mathbf{k}^{(s)}$ it is the density matrix that changes the fastest, we can approximate

$$\mathbf{j}(t)\approx\sum_{mns}\frac{V_s}{(2\pi)^3}O_{nm}(\mathbf{k}^{(s)}-\mathbf{A}(t))\int_{V_s}\frac{d\mathbf{k}}{V_s}\rho_{mn}(\mathbf{k}|t) \ . \quad (24)$$

In this approximation, we need to replace the grid-sample $\rho_{mn}(\mathbf{k}^{(s)}|t)$, which is used in the straightforward grid-based sampling (21), with the average of the density matrix over the cell V_s:

$$\rho_{mn}(\mathbf{k}^{(s)}|t) \to \bar{\rho}_{mn}(s|t) \equiv \int_{V_s}\frac{d\mathbf{k}}{V_s}\rho_{mn}(\mathbf{k}|t) \ . \quad (25)$$

To express the average of the density matrix over V_s in terms of the quantities from the previous time step, we write

$$\bar{\rho}_{mn}(s|t_{i+1}) = \int_{V_s}\frac{d\mathbf{k}}{V_s}\rho_{mn}(\mathbf{k}|t_{i+1}), \quad (26)$$

and with the help of the evolution operator (16) as

$$\bar{\rho}_{mn}(s|t_{i+1}) = \int_{V_s}\frac{d\mathbf{k}}{V_s}\sum_{a,b}e^{-i\epsilon_m(\mathbf{k}_i)\Delta t}\ U^{(i)}_{ma}(\mathbf{k})\rho_{ab}(\mathbf{k}|t_i)(U^{(i)}(\mathbf{k}))^{\dagger}_{an}\ e^{+i\epsilon_n(\mathbf{k}_i)\Delta t} \ . \quad (27)$$

At this point we make yet another approximation assuming that the exponentials in the above integrand are the fastest phase-changing terms. Approximating all other terms by their values at $\mathbf{k} = \mathbf{k}^{(s)}$, we obtain

$$\bar{\rho}_{mn}(s|t_{i+1}) = \sum_{a,b}U^{(i)}_{ma}(\mathbf{k}^{(s)})\rho_{ab}(\mathbf{k}^{(s)}|t_i)(U^{(i)}(\mathbf{k}^{(s)}))^{\dagger}_{an}\ \int_{V_s}\frac{d\mathbf{k}}{V_s}e^{-i\epsilon_m(\mathbf{k})\Delta t}\ e^{+i\epsilon_n(\mathbf{k})\Delta t} \ , \quad (28)$$

or equivalently

$$\bar{\rho}_{mn}(s|t_{i+1}) = \rho_{mn}(\mathbf{k}^{(s)}|t_{i+1})\int_{V_s}\frac{d\mathbf{k}}{V_s}e^{-i(\epsilon_m(\mathbf{k})-\epsilon_m(\mathbf{k}^{(s)}))\Delta t}\ e^{+i(\epsilon_n(\mathbf{k})-\epsilon_n(\mathbf{k}^{(s)}))\Delta t} \ . \quad (29)$$

Finally, we Taylor-expand the energy differences in the exponential up to the first order, for example

$$(\epsilon_m(\mathbf{k}) - \epsilon_m(\mathbf{k}^{(s)})) \approx (\mathbf{k} - \mathbf{k}^{(s)}) \; . \; \frac{\partial \epsilon_m(\mathbf{k}^{(s)})}{\partial \mathbf{k}^{(s)}} \; , \qquad (30)$$

so that the integral can be evaluated and we obtain

$$\bar{\rho}_{mn}(s|t_{i+1}) = \rho_{mn}(\mathbf{k}^{(s)}|t_{i+1}) \prod_{d=1}^{3} \mathrm{sinc}\left[\Delta t/\tau_{ab}^{(d)}\right] \qquad (31)$$

with

$$\left(\tau_{ab}^{(d)}\right)^{-1} \approx \frac{1}{2N} \mathbf{b}_d . \left[\frac{\partial \epsilon_b(\mathbf{k})}{\partial \mathbf{k}} - \frac{\partial \epsilon_a(\mathbf{k})}{\partial \mathbf{k}}\right]\Bigg|_{\mathbf{k}=\mathbf{k}^{(s)}} \; . \qquad (32)$$

So if we decide that our grid samples of the density matrix represent the average values of the corresponding grid-cells, we arrive at an evolution scheme in which the sgiSBEs algorithm become augmented by an additional split-step

$$\rho_{mn}(\mathbf{k}^{(s)}|t) \leftarrow \rho_{mn}(\mathbf{k}^{(s)}|t) \prod_{d=1}^{3} \mathrm{sinc}\left[\Delta t/\tau_{ab}^{(d)}\right] \; . \qquad (33)$$

This is a generalization of the usual phenomenological dephasing split-step

$$\rho_{mn}(\mathbf{k}^{(s)}|t) \leftarrow \rho_{mn}(\mathbf{k}^{(s)}|t) \exp\left[-\Delta t/T_2\right] \; , \qquad (34)$$

but with a band-dependent dephasing time which reflects the discreteness of the $\mathbf{k}$-grid (via N in Eqn. (32)). Obviously, the approximations we have committed only make sense if the grid-spacing is small, and it means that the arguments of the sinc functions must also be very small.

It is clear that in the limit of very small integration step $\Delta t \to 0$ and for a fine grid $N \to \infty$ we recover the simple sampling method of (21). So the grid-induced dephasing (33) does not represent any new physical mechanism, it is merely a tool to accelerate the convergence with respect to N.

There are a number of places at which we have neglected the dependence on $\mathbf{k}$, so it will be interesting to explore if (33) could be refined to further improve the convergence.

[1] S. Ghimire, A. D. DiChiara, E. Sistrunk, P. Agostini, L. F. DiMauro, and D. A. Reis, Observation of high-order harmonic generation in a bulk crystal, Nature Physics **7**, 138 (2011).

[2] E. Goulielmakis and T. Brabec, High harmonic generation in condensed matter, Nature Photonics **16**, 411 (2022).

[3] J. Park, A. Subramani, S. Kim, and M. F. Ciappina, Recent trends in high-order harmonic generation in solids, Advances in Physics: X **7**, 2003244 (2022).

[4] L. Yue and M. B. Gaarde, Introduction to theory of high-harmonic generation in solids: tutorial, J. Opt. Soc. Am. B **39**, 535 (2022).

[5] M. T. Schlecht, M. Knorr, C. P. Schmid, S. Malzer, R. Huber, and H. B. Weber, Light-field-driven electronics in the mid-infrared regime: Schottky rectification, Science Advances **8**, 5014 (2022),.

[6] G. Vampa, T. J. Hammond, N. Thiré, B. E. Schmidt, F. Légaré, C. R. McDonald, T. Brabec, D. D. Klug, and P. B. Corkum, All-optical reconstruction of crystal band structure, Phys. Rev. Lett. **115**, 193603 (2015).

[7] J. Chen, Q. Xia, and L. Fu, Reconstruction of crystal band structure by spectral caustics in high-order harmonic generation, Phys. Rev. A **104**, 063109 (2021).

[8] A. A. Lanin, E. A. Stepanov, A. B. Fedotov, and A. M. Zheltikov, Mapping the electron band structure by intraband high-harmonic generation in solids, Optica **4**, 516 (2017).

[9] T. T. Luu and H. J. Wörner, Measurement of the berry curvature of solids using high-harmonic spectroscopy, Nature Communications **9**, 916 (2018).

[10] U. Lindefelt, H.-E. Nilsson, and M. Hjelm, Choice of wavefunction phases in the equations for electric-field-induced interband transitions, Semiconductor Science and Technology **19**, 1061 (2004).

[11] S. Jiang, C. Yu, J. Chen, Y. Huang, R. Lu, and C. D. Lin, Smooth periodic gauge satisfying crystal symmetry and periodicity to study high-harmonic generation in solids, Phys. Rev. B **102**, 155201 (2020).

[12] O. Schubert, M. Hohenleutner, F. Langer, B. Urbanek, C. Lange, U. Huttner, D. Golde, T. Meier, M. Kira, S. W. Koch, and R. Huber, Sub-cycle control of terahertz high-harmonic generation by dynamical bloch oscillations, Nature Photonics **8**, 119 (2014).

[13] J. Gu and M. Kolesik, Full-brillouin-zone calculation of high-order harmonic generation from solid-state media, Phys. Rev. A **106**, 063516 (2022).

[14] I. Floss, C. Lemell, G. Wachter, V. Smejkal, S. A. Sato, X.-M. Tong, K. Yabana, and J. Burgdörfer, Ab initio multiscale simulation of high-order harmonic generation in solids, Phys. Rev. A **97**, 011401 (2018).

[15] G. G. Brown, A. Jiménez-Galán, R. E. F. Silva, and M. Ivanov, A real-space perspective on dephasing in solid-state high harmonic generation, arXiv:2210.16889 (2022).

[16] H. Haug and S. W. Koch, *Quantum Theory of the Optical and Electronic Properties of Semiconductors* (World Scientific Publishing, Singapore, 2009).

[17] J. Wilhelm, P. Grössing, A. Seith, J. Crewse, M. Nitsch, L. Weigl, C. Schmid, and F. Evers, Semiconductor bloch-equations formalism: Derivation and application to high-harmonic generation from dirac fermions, Phys. Rev. B **103**, 125419 (2021).

[18] M. Hohenleutner, F. Langer, O. Schubert, M. Knorr, U. Huttner, S. Koch, M. Kira, and R. Huber, Real-time observation of interfering crystal electrons in high-harmonic generation, Nature **523**, 572 (2015).

[19] G. Vampa, C. R. McDonald, G. Orlando, D. D. Klug,

P. B. Corkum, and T. Brabec, Theoretical analysis of high-harmonic generation in solids, Phys. Rev. Lett. **113**, 073901 (2014).
[20] C. Yu, X. Zhang, S. Jiang, X. Cao, G. Yuan, T. Wu, L. Bai, and R. Lu, Dependence of high-order-harmonic generation on dipole moment in SiO_2 crystals, Phys. Rev. A **94**, 013846 (2016).
[21] T. T. Luu and H. J. Wörner, High-order harmonic generation in solids: A unifying approach, Phys. Rev. B **94**, 115164 (2016).
[22] S. Jiang, J. Chen, H. Wei, C. Yu, R. Lu, and C. D. Lin, Role of the transition dipole amplitude and phase on the generation of odd and even high-order harmonics in crystals, Phys. Rev. Lett. **120**, 253201 (2018).
[23] S. Jiang, H. Wei, J. Chen, C. Yu, R. Lu, and C. D. Lin, Effect of transition dipole phase on high-order-harmonic generation in solid materials, Phys. Rev. A **96**, 053850 (2017).
[24] Y. S. You, Y. Yin, Y. Wu, A. Chew, X. Ren, F. Zhuang, S. Gholam-Mirzaei, M. Chini, Z. Chang, and S. Ghimire, High-harmonic generation in amorhous solids, Nature Comm. **8**, 724 (2017).
[25] X. Zhang, J. Li, Z. Zhou, S. Yue, H. Du, L. Fu, and H.-G. Luo, Ellipticity dependence transition induced by dynamical bloch oscillations, Phys. Rev. B **99**, 014304 (2019).
[26] D. Wu, L. Li, Y. Zhan, T. Huang, H. Cui, J. Li, P. Lan, and P. Lu, Determination of transition dipole moments of solids with high-order harmonics driven by multicycle ultrashort pulses, Phys. Rev. A **105**, 063101 (2022).
[27] Y. Qiao, Y.-Q. Huo, S.-C. Jiang, Y.-J. Yang, and J.-G. Chen, All-optical reconstruction of three-band transition dipole moments by the crystal harmonic spectrum from a two-color laser pulse, Opt. Express **30**, 9971 (2022).
[28] S. S. Prabhu, S. E. Ralph, M. R. Melloch, and E. S. Harmon, Carrier dynamics of low-temperature-grown GaAs observed via THz spectroscopy, Applied Physics Letters **70**, 2419 (1997).
[29] P. Xia, C. Kim, F. Lu, T. Kanai, H. Akiyama, J. Itatani, and N. Ishii, Nonlinear propagation effects in high harmonic generation in reflection and transmission from gallium arsenide, Opt. Express **26**, 29393 (2018).
[30] P. Xia, T. Tamaya, C. Kim, F. Lu, T. Kanai, N. Ishii, J. Itatani, H. Akiyama, and T. Kato, High-harmonic generation in GaAs beyond the perturbative regime, Phys. Rev. B **104**, L121202 (2021).
[31] F. Langer, M. Hohenleutner, C. P. Schmid, C. Poellmann, P. Nagler, T. Korn, C. Schüller, M. S. Sherwin, U. Huttner, J. T. Steiner, S. W. Koch, M. Kira, and R. Huber, Lightwave-driven quasiparticle collisions on a subcycle timescale, Nature **533**, 225 (2016).
[32] I. Kilen, S. W. Koch, J. Hader, and J. V. Moloney, Fully microscopic modeling of mode locking in microcavity lasers, J. Opt. Soc. Am. B **33**, 75 (2016).
[33] I. Kilen, M. Kolesik, J. Hader, J. V. Moloney, U. Huttner, M. K. Hagen, and S. W. Koch, Propagation induced dephasing in semiconductor high-harmonic generation, Phys. Rev. Lett. **125**, 083901 (2020).
[34] G. Wang and T.-Y. Du, Quantum decoherence in high-order harmonic generation from solids, Phys. Rev. A **103**, 063109 (2021).
[35] T.-Y. Du and C. Ma, Temperature-induced dephasing in high-order harmonic generation from solids, Phys. Rev. A **105**, 053125 (2022).
[36] D. Freeman, A. Kheifets, S. Yamada, A. Yamada, and K. Yabana, High-order harmonic generation in semiconductors driven at near- and mid-infrared wavelengths, Phys. Rev. B **106**, 075202 (2022).
[37] C. Q. Abadie, M. Wu, and M. B. Gaarde, Spatiotemporal filtering of high harmonics in solids, Opt. Lett. **43**, 5339 (2018).
[38] S. Han, L. Ortmann, H. Kim, Y. W. Kim, T. Oka, A. Chacon, B. Doran, M. Ciappina, M. Lewenstein, S.-W. Kim, S. Kim, and A. S. Landsman, Extraction of higher-order nonlinear electronic response in solids using high harmonic generation, Nature Communications **10**, 3272 (2019).
[39] J. Gu, A. Schweinsberg, L. Vanderhoef, M. Tripepi, A. Valenzuela, C. Wolfe, T. R. Ensley, E. Chowdhury, and M. Kolesik, Random quasi-phase-matching in polycrystalline media and its effects on pulse coherence properties, Opt. Express **29**, 7479 (2021).
[40] S. Vasilyev, J. Gu, M. Mirov, Y. Barnakov, I. Moskalev, V. Smolski, J. Peppers, M. Kolesik, S. Mirov, and V. Gapontsev, Low-threshold supercontinuum generation in polycrystalline media, J. Opt. Soc. Am. B **38**, 1625 (2021).
[41] Y.-L. He, J. Guo, F.-Y. Gao, Z.-J. Yang, S.-Q. Zhang, and X.-S. Liu, Interference between harmonics of different crystal momentum channels in solid high-order harmonic generation, Phys. Rev. A **104**, 013104 (2021).
[42] H. F. Johnson, Comp. Phys. Comm. **43**, 181 (1987).
[43] A. Couairon, E. Brambilla, T. Corti, D. Majus, O. d. J. Ramírez-Góngora, and M. Kolesik, Practitioner's guide to laser pulse propagation models and simulation, Eur. Phys. J. Special Topics **199**, 5 (2011).
[44] P. Vogl, H. P. Hjalmarson, and J. D. Dow, A semi-empirical tight-binding theory of the electronic structure of semiconductors†, Journal of Physics and Chemistry of Solids **44**, 365 (1983).
[45] M. Kolesik, Assessment of tight-binding models for high-harmonic generation in zinc blende materials, Opt. Lett. **48**, 3191 (2023).
[46] A. J. Uzan, G. Orenstein, A. Jiménez-Galán, C. McDonald, R. E. F. Silva, B. D. Bruner, N. D. Klimkin, V. Blanchet, T. Arusi-Parpar, M. Krüger, A. N. Rubtsov, O. Smirnova, M. Ivanov, B. Yan, T. Brabec, and N. Dudovich, Attosecond spectral singularities in solid-state high-harmonic generation, Nature Photonics **14**, 183 (2020).
[47] T. Hansen, S. V. B. Jensen, and L. B. Madsen, Correlation effects in high-order harmonic generation from finite systems, Phys. Rev. A **105**, 053118 (2022).